Title
Distribution and energy balance of Pluto’s nitrogen ice, as seen by New Horizons in 2015

Authors
Lewis, Briley L
Stansberry, John A
Holler, Bryan J
et al.

Publication Date
2021-03-01

DOI
10.1016/j.icarus.2020.113633

Distribution and Energy Balance of Pluto's Nitrogen Ice, as seen by New Horizons in 2015

Briley L. Lewis[a,b,**], John A. Stansberry[c,*], Bryan J. Holler[c], William M. Grundy[d], Bernard Schmitt[e], Silvia Protopapa[f], Carey Lisse[h], S. Alan Stern[g], Leslie Young[g], Harold A. Weaver[h], Catherine Olkin[g], Kimberly Ennico[i], and the New Horizons Science Team

[a] *Department of Astronomy, Columbia University, 550 W. 120th St., New York, NY 10027*
[b] *Division of Astronomy and Astrophysics, University of California, Los Angeles, 475 Portola Plaza, Los Angeles, CA 90025*
[c] *Space Telescope Science Institute, 3700 San Martin Drive, Baltimore, MD 21218*
[d] *Lowell Observatory, 1400 W Mars Hill Rd, Flagstaff, AZ 86001*
[e] *Université Grenoble Alpes, France*
[f] *Department of Astronomy, University of Maryland, College Park, College Park, MD 20742-2421*
[g] *Southwest Research Institute,1050 Walnut St 300, Boulder, CO 80302*
[h] *Johns Hopkins University Applied Physics Laboratory, 11100 Johns Hopkins Rd, Laurel, MD 20723*
[i] *NASA Ames Research Center, Moffett Blvd, Mountain View, CA 94035*

Abstract

Pluto's surface is geologically complex because of volatile ices that are mobile on seasonal and longer time scales. Here we analyzed New Horizons LEISA spectral data to globally map the nitrogen ice, including nitrogen with methane diluted in it. Our goal was to learn about the seasonal processes influencing ice redistribution, to calculate the globally averaged energy balance, and to place a lower limit on Pluto's N_2 inventory. We present the average latitudinal distribution of nitrogen and investigate the relationship between its distribution and topography on Pluto by using maps that include the shifted bands of methane in solid solution with nitrogen (which are much stronger than the 2.15- μm nitrogen band) to more completely map the distribution of the nitrogen ice. We find that the global average bolometric albedo is 0.83 ± 0.11, similar to that inferred for Triton, and that a significant fraction of Pluto's N_2 is stored in Sputnik Planitia. We also used the encounter-hemisphere distribution of nitrogen ice to infer the latitudinal distribution of nitrogen over the rest of Pluto, allowing us to calculate the global energy balance. Under the assumption that Pluto's nitrogen-dominated 11.5 μbar atmosphere is in vapor pressure equilibrium with the nitrogen ice, the ice temperature is 36.93 ± 0.10 K, as measured by New Horizons' REX instrument. Combined with our global energy balance calculation, this implies that the average bolometric emissivity of Pluto's nitrogen ice is probably in the range 0.47 – 0.72. This is consistent with the low emissivities estimated for Triton based on Voyager results, and may have implications for Pluto's atmospheric seasonal variations, as discussed below. The global pattern of volatile transport at the time of the encounter was from north to south, and the transition between condensation and sublimation within Sputnik Planitia is correlated with changes in the grain size and CH_4 concentration derived from the spectral maps. The low emissivity of Pluto's N_2 ice suggests that Pluto's atmosphere may undergo an extended period of constant pressure even as Pluto recedes from the Sun in its orbit.

Keywords:
Pluto; Pluto: surface; Pluto: atmosphere; Pluto: albedo; Volatile; Emissivity

1. Introduction

Pluto's atmosphere was discovered in 1988 via stellar occultation (Hubbard et al., 1988; Elliot et al., 1989), and with the discovery of N_2 ice on its surface, it became apparent that the atmosphere was likely dominated by N_2 (not CH_4) in vapor pressure equilibrium with the ice (*e.g.* Owen et al. 1993). Due to the large latent heat of sublimation of N_2, sublimation and condensation efficiently re-distribute energy from highly-illuminated to less-illuminated (or dark) regions, with the result that the N_2 ice everywhere is essentially isothermal (*e.g.* Spencer et al. 1997, Trafton and Stern 1983). This is also true for Triton's atmosphere (*e.g.* Yelle et al. 1995, Trafton 1984). However, because New Horizons included a mapping spectrometer (while Voyager did not) we now know in detail how the N_2 ice is distributed on Pluto (but not on Triton). Thus we can relate the N_2 (and CO and CH_4) ice distribution to the stunning diversity of terrain on Pluto's surface revealed by New Horizons in 2015. We can also use the measured distribution of N_2 to calculate its energy balance, without the need to simply assume a relationship between albedo and composition as was necessary for Triton (*e.g.* Stansberry et al. 1992). New Horizons also revealed that topography can strongly influence the distribution of volatile ices, namely that the Sputnik Planitia basin is filled with N_2, CH_4, and CO (as described in Grundy et al. (2016)). That relationship was not understood based on Voyager observations of Triton (in part because of the very subdued topography there), but was predicted prior to the Pluto encounter (Stansberry et al., 2014; Trafton and Stansberry, 2015), and further described post-encounter (Bertrand and Forget, 2016).

Data from the Linear Etalon Imaging Spectral Array (LEISA) and Multi-spectral Visible Imaging Camera (MVIC) provided global views of composition, albedo, color and geology on Pluto (Reuter et al., 2008; Stern, 2010). In addition, the Long-Range Reconnaisance Imager (LORRI, Cheng et al. (2008)) provided albedo and limited geologic information at long ranges, particularly of Pluto's Charon-facing hemisphere, which was also not visible at New Horizons' closest approach. In this study, we used previously published maps created from LEISA data to create new global maps of Pluto's nitrogen-ice deposits. We then combined these maps with existing albedo data and topographic maps to investigate correlations between nitrogen presence and insolation and topography, estimate the N_2 ice bolometric albedo and emissivity, and describe how the N_2 distribution varies with latitude.

Our goal was to use the New Horizons data sets to provide the most comprehensive map of N_2 ice distribution on Pluto, relate that distribution to the geology (specifically topography), and precisely determine the global energy balance of that ice. These results

*Corresponding author
**Primary corresponding author
Email address: bll2124@columbia.edu (Briley L. Lewis)
URL: jstans@stsci.edu (John A. Stansberry)

provide a detailed snapshot of Pluto's seasonal and climatic state at the epoch of the New Horizons encounter. Future modeling work that investigates the seasonal evolution of the volatile ice distribution and atmospheric pressure and composition of Pluto can use our results as a starting point for predictions, or as a constraint informing historical studies. Previous studies have presented maps of the N_2 ice distribution on the encounter hemisphere, based on the presence of the 2.15- μm absorption band and CH_4 band shift, as well as maps for H_20, CO and CH_4 ices and tholins (Grundy et al., 2016; Protopapa et al., 2017; Schmitt et al., 2017; Stern, 2010; Stern et al., 2015), and for CH_4 only (Earle et al., 2017). Some of these additional maps are used in our investigations of volatile abundance at various elevations in Section 2.2. Topographic data was also limited to the encounter (*i.e.* anti-Charon) hemisphere of Pluto, because it requires high resolution imagery, and is based on the digital elevation model (DEM) of Schenk et al. (2018). We also relied on maps of bolometric albedo (Buratti et al., 2017), which cover both the encounter and sub-Charon hemispheres of Pluto, albeit at vastly different spatial resolution. All of these data products are limited to the illuminated latitudes of Pluto at the encounter epoch, *i.e.* northward of 38°S (except for some limited topographic information in the "haze-illuminated" region south of the terminator on the encounter hemisphere – see Schenk et al. 2018; Stern 2010).

Another critical constraint is provided by the measurement of Pluto's atmospheric surface pressure. Because the N_2-dominated atmosphere and surface N_2 ices are in effective vapor pressure equilibrium, the atmospheric surface pressure can be equated to the physical temperature (as distinguished from the brightness temperature, such as was measured using the REX instrument) of the N_2 ice via the vapor pressure relation. Hinson et al. (2017), based on the REX radio-occultation results from ingress and egress, give a mean atmospheric surface pressure of $11.5 \pm 0.7\,\mu$bar, at a radius of 1189 km (within 1 km of Pluto's average radius, 1188.3 ± 1.6 km; Nimmo et al. 2017). Using the older vapor pressure curve of Brown and Ziegler (1980), this implies a N_2-ice temperature of 37.18 ± 0.10 K. However, Fray and Schmitt (2009) find that the vapor pressure over N_2 ice is actually $\simeq 18\%$ higher at these temperatures, implying a N_2-ice temperature of 36.93 ± 0.10 K. We adopt the Fray and Schmitt (2009) results for the remainder of this paper. The small temperature error is a result of the steep dependence of the vapor pressure on temperature (*i.e.* of the large latent heat of sublimation of N_2). The REX instrument also obtained brightness temperature measurements for Pluto's near-surface at a wavelength of 4.2 cm. Interpretation of those data in terms of the physical temperature of the surface, and specifically of areas covered in N_2 ice, is ongoing, but seem to require a (non-bolometric) emissivity near 0.7 for Sputnik Planitia[1] (Linscott *et al.*, submitted.) We return to the topic of the emissivity of Pluto's N_2 ice below.

Methane and N_2 ices coexist as dilute solid solutions with one another. As reviewed by Trafton (2015), the maximum CH_4 and N_2 mixing ratios in the other ice are 4% and 3%, respectively, at 37 K. Individual ice grains are thus either N_2 dominated (N_2:CH_4) or CH_4 dominated (CH_4:N_2). If the bulk composition of the ice in a particular location has a CH_4 mixing ratio in the range 4% – 97%, that ice is an assemblage of CH_4 grains saturated in N_2 and of N_2 grains saturated in CH_4. The solution between these species will affect their vapor pressures, and is expected to result in non-ideal vapor pressure behavior (*i.e.*

[1]Some place names on Pluto are a mix of informal and officially approved names.

not obeying Raoult's law: $P_{N_2}^{Sat} = X_{N_2} \times P_{N_2}^{Vap}$). Trafton (2015) shows that the vapor pressure of N_2 over an assemblage of grains of saturated N_2:CH_4 could be significantly lower than the Rauolt's law prediction. However, laboratory data constraining the vapor pressure behavior is lacking, so it is currently unknown how much the vapor pressure of N_2 is depressed (nor how much the vapor pressure of CH_4 over saturated CH_4:N_2 is increased). There are now theoretical equations of state available, but they have yet to be validated by data, and thus were not included in this analysis. Lacking specific information on these effects, we assumed that Pluto's N_2:CH_4 ice behaves very much like N_2 ice, and CH_4:N_2 behaves very much like CH_4 ice, in terms of vapor pressure (with application to determining the surface pressure of the N_2-dominated atmosphere) and sublimation and condensation (with application to volatile transport rates and global redistribution of insolation via latent heat transport).

In Section 2, we explain the methods used to create new maps of the distribution of N_2 ice needed for this investigation, and how elevation relates to the distribution of this volatile. Then, in Section 3, we calculate the emissivity required to produce an ice temperature of 37 K using principles of energy balance, utilizing our global nitrogen maps, bolometric albedo maps based on LORRI data (Cheng et al., 2008) and the results of Buratti et al. (2017), and assumed N_2-ice scenarios for the unobserved South Pole. Lastly, Section 4 explores the possible physical causes of the observed trends and the implications of our energy balance calculations, drawing on other long-term volatile transp.pngort and climate modeling efforts from the New Horizons team.

2. Geographic and Topographic Distributions of Volatile Ices

2.1. Global Composition Maps and the Distribution of N_2 Ice

Data from the LEISA spectral imager were previously analyzed to derive detailed spectral maps for Pluto's encounter hemisphere. The LEISA spectra cover wavelengths from 1.25-2.5 μm, with a spectral resolving power $\lambda/\Delta\lambda \simeq 240$ (Reuter et al., 2008). Multiple absorption features of CH_4 CO and H_2O ices are present in that wavelength range, as is the overtone band of N_2 ice at 2.15-μm. The encounter hemisphere data from LEISA have typical spatial resolution of 6 to 7 km per pixel (Grundy et al., 2016). There are two main approaches to interpreting those data: directly measuring integrated band depths from the spectra, and fitting spectral models.

Integrated band depth maps (Schmitt et al., 2017) directly measure the strength of selected absorption features. The approach used in that study enabled removal of some instrumental artifacts (via principle component analysis) not corrected by the data pipeline. The resulting maps retained the full spatial resolution of the LEISA data. Because the weak 2.15-μmN_2 band occurs at wavelengths co-incident with the much stronger 2.2-μmCH_4 band, the strength of the 2.15-μmN_2 band is quite sensitive to the presence of CH_4. In areas with a particularly high abundance of CH_4, it becomes very difficult to discern the N_2 absorption.Figure 1 (top) shows the N_2 band depth map of Schmitt et al. (2017). For our energy balance calculations, we used a new binary map of N_2 distribution based on both the observed 2.15-μm band depth and the presence of shifted bands of CH_4 diluted in N_2 (B. Schmitt, in preparation). This map does not have information on the strength of the N_2 signatures, but instead provides information on whether or not N_2 is present in a particular pixel. For the topographic investigation

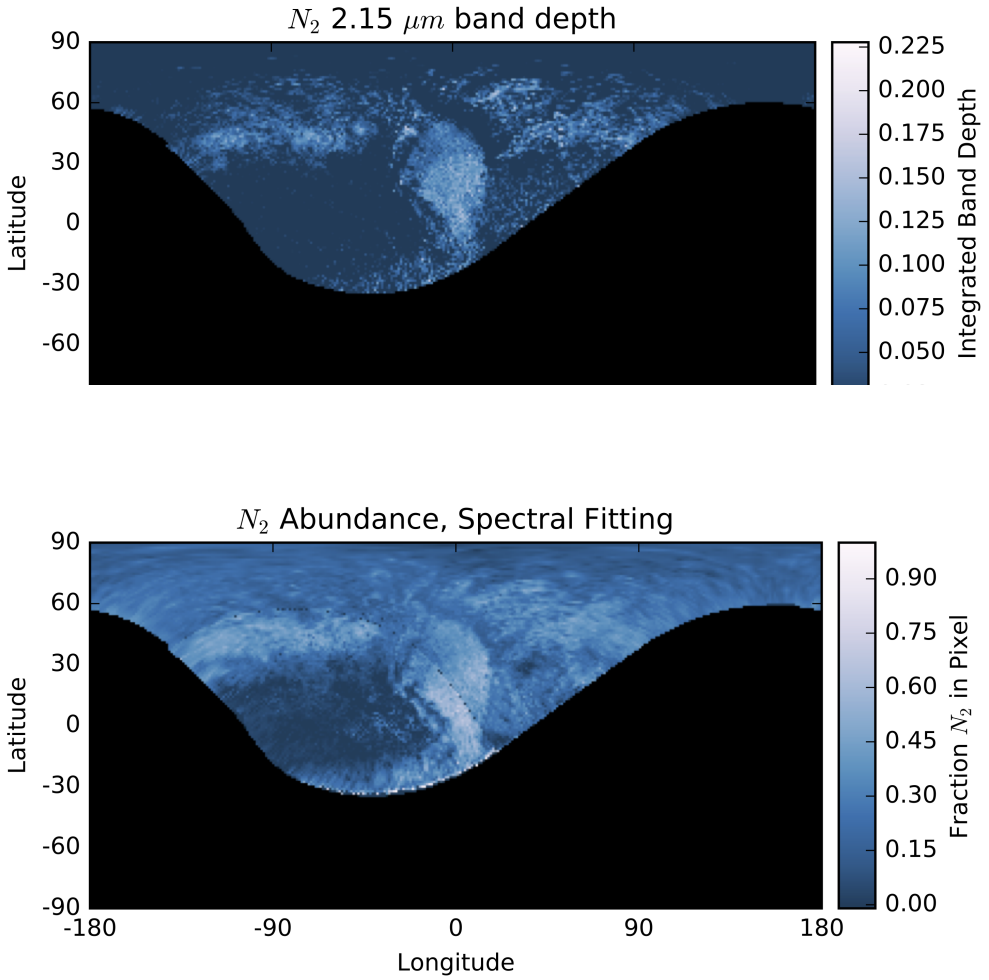

Figure 1: Previously published maps of N_2 ice distribution. Top: Map of the 2.15-μm feature band depth from Schmitt et al. (2017). Bottom: Abundance of N_2-enriched component from the spectral model fits of Protopapa et al. (2017). Those fits are strongly influenced by the N_2 ice 2.15-μm feature, and also include the effects of multiple shifted bands of CH_4 dissolved in N_2 ice.

(Section 2.2), we used the band depth only map from Schmitt et al. (2017), with a detection threshold of 0.005.

By fitting spectral models to the data, it is possible to simultaneously map N_2 and CH_4, even in areas where the CH_4 absorption is very strong. Protopapa et al. (2017) fit Hapke spectral models to the LEISA encounter-hemisphere data. That approach is computationally expensive, so the models were fit to data that were spatially binned by a factor of 4 (giving maps with a resolution of 24 – 28 km). These maps can provide more information about the distribution of the spectral components included in the models (N_2, CH_4, H_2O and tholin), including the fractional abundance and grain size (related to the apparent path length) of each spectral component within each (binned) pixel.

To determine the albedo and energy balance of just areas with N_2-ice deposits, we required an accurate map of the N_2 distribution on Pluto's surface. To accomplish this, we dealt with two main challenges: reconciling the band depth maps and the spectral modeling maps, including their spatial-resolution differences, and extrapolating the measured N_2 distribution to fill in areas beyond the encounter hemisphere and areas on Pluto that were un-illuminated at the time of the encounter.

Firstly, we re-sampled the Protopapa et al. (2017) spectral modeling maps to match the resolution of the Schmitt et al. (2017) integrated band depth maps and qualitative N_2 abundance maps. This is equivalent to assuming that the entire pixel in the lower resolution maps of (Protopapa et al., 2017) contains some of the species (N_2:CH_4) being mapped. We then combined the maps to create a map of N_2 ice distribution, as follows. If a pixel in either of the maps (binary observed N_2 distribution, N_2 abundance from spectral modeling) indicated nitrogen presence, that pixel in our final map was set to 1. For the band depth maps, the acceptable band depth range to indicate nitrogen presence is a value greater than or equal to 0.005. These band depth maps were only used for the investigation in Section 2.2. For all energy balance calculations, we used the binary N_2 map that includes N_2 detected by both the CH_4 band shift and the 2.15-μm N_2 feature. For the spectral modeling maps, any N_2 abundance above 0.0 indicates presence. Areas without nitrogen present in any of the maps were set to 0. This approach provides a more complete and detailed map of the presence of N_2 ice on Pluto, but may still underestimate the total inventory because of the weakness of the 2.15- μm band and finite sensitivity of the data.

To fill in our N_2 map in areas outside the encounter hemisphere, for which no composition maps have yet been created, and where spatial resolution will be much lower, we adopted a scheme of fractional abundances. On the encounter hemisphere, for each degree of latitude, we counted all pixels covered by nitrogen and divided that by the total number of pixels for which we had data, providing a fraction of the surface that is covered at that latitude, as shown in the bottom panel of Figure 2. We then created a random distribution with the same fraction of pixels covered and inserted that into the no-data areas at that latitude bin to create a global map of nitrogen presence, as shown in the top panel of Figure 2. When calculating the fractional coverage at a given latitude, we excluded pixels falling within Sputnik Planitia. As described below, the process responsible for the N_2 deposit in S.P. is driven by topography, not seasonal nor climatic effects that should produce latitudinal patterns in the ice distribution. There is no evidence for such large impact basins to be present on the the Charon-facing hemisphere of Pluto (Grundy et al., 2010; Stern, 2010), so including S.P. in our calculation of the latitudinal distribution of N_2 would have biased our result. The resulting map of N_2 ice on Pluto is

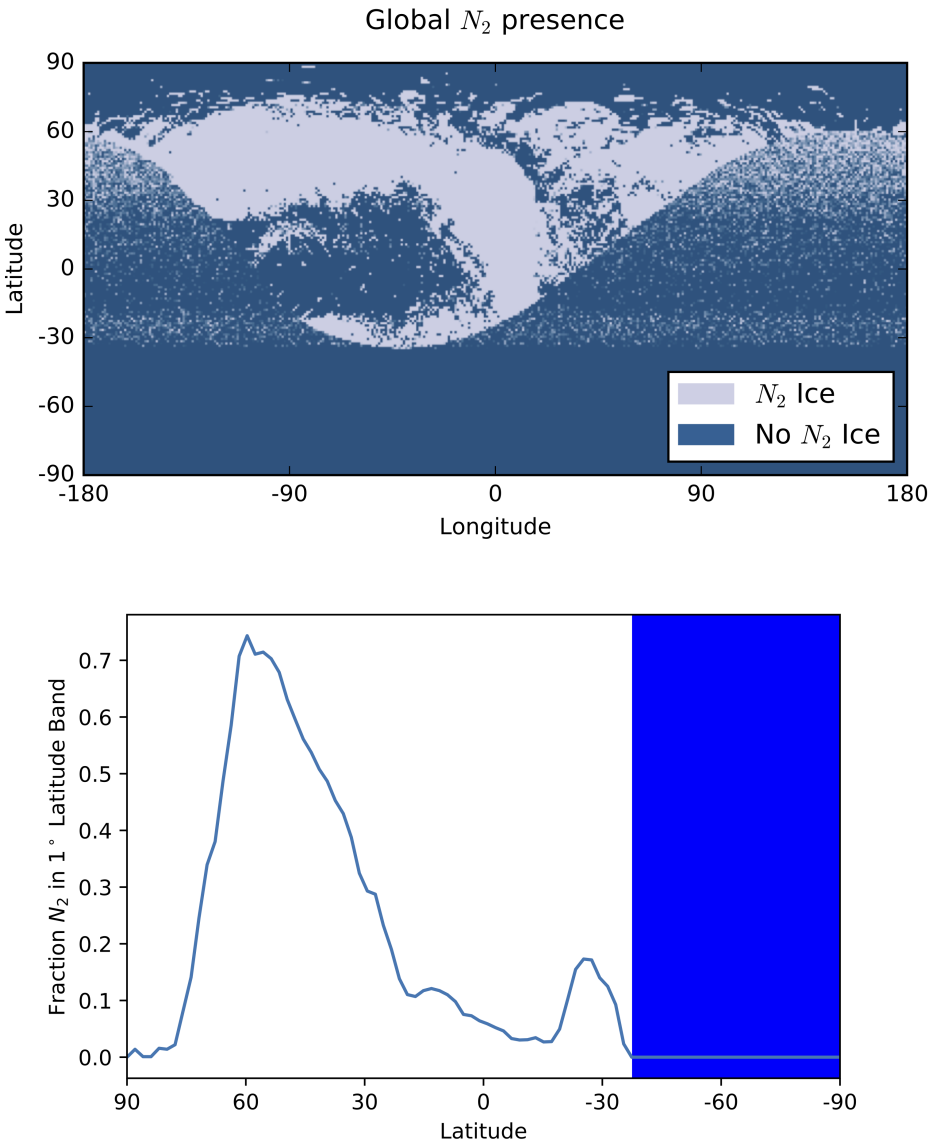

Figure 2: (Top) Binary map of nitrogen presence on Pluto based on the results of Protopapa et al. (2017) and Schmitt et al. (2017) (shown in 1). The non-encounter hemisphere sections (no-data areas) are filled in by matching the fractional abundance at that latitude, as described in Section 2.1. Areas south of approximately 38°S also have no available data. Here we show that area as being devoid of N_2 ice, but in Section 3.1 we explore the implications of different assumptions about N_2 ice coverage in the un-illuminated southern regions. (Bottom) Map of latitudinal dependence of Nitrogen ice coverage. Values listed are the fractional abundance of nitrogen ice in each 1 degree latitude bin (e.g. how many pixels of the LEISA data contain the signal of nitrogen out of the total number of pixels in that latitude band). Areas below 38°S were unilluminated, so the amount of N_2 ice there is unknown.

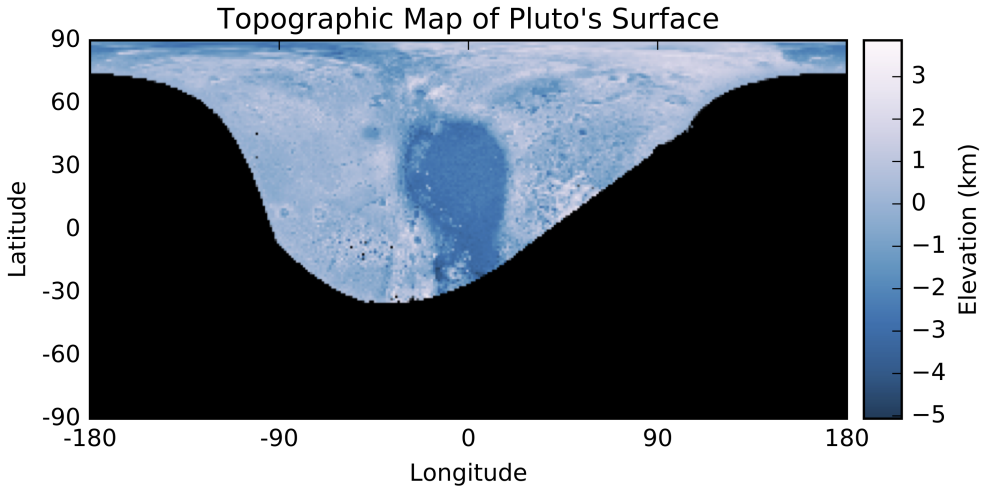

Figure 3: Previously published topographic map of Pluto's encounter hemisphere (Schenk et al., 2018). The prominent Sputnik Planitia basin near map center dominates the topography. The elevation data are defined such that elevations of 0 km are at the the mean planetary radius.

given in Figure 2, top panel.

2.2. Elevation and Volatile Ice Distribution

Vapor pressure equilibrium has long been understood to govern the atmospheric pressure of Pluto (and similar bodies, Triton certainly, and perhaps Eris, Sedna, and Makemake at their warmer seasons). The concept of vapor pressure equilibrium between global N_2 ice deposits and Pluto's global-scale atmosphere is complicated by the fact that the N_2 occurs at a range of elevations (or more precisely, geopotential radii). As pointed out by Stansberry et al. (2014) and Trafton and Stansberry (2015), this produces an additional term that causes the N_2 ice at higher elevations (lower atmospheric pressure) to sublimate, and for condensation of N_2 ices to be favored at lower elevations (higher atmospheric pressure), other aspects governing the energy balance of the ice being equal. This basic physical process of downward volatile transport is also confirmed by global climate models of Pluto's surface and atmosphere (Bertrand and Forget, 2016). So, Pluto's atmosphere is characterized by both a global vapor pressure equilibrium temperature (T_{N_2}) and equivalent surface pressure (P_{N_2}), and by a global vapor pressure equilibrium radius or elevation (Z_{N_2}). Any N_2 ice at elevations other than Z_{N_2} will tend to undergo downward topography-driven volatile transport.

The correlation of the huge deposit of N_2, CO and CH_4 ice that makes up Sputnik Planitia with low elevations was noted by Grundy et al. (2016), and is readily apparent by comparing Figures 1 and 3. Topography-driven volatile transport of N_2 on Pluto

is relatively slow (for elevation differences of a few km) compared to seasonal transport. This is because topography-driven transport is energy-limited by the difference in thermal emission at T_{N_2} and at temperatures given by the wet adiabatic lapse rate at elevations other than Z_{N_2}. The balance between insolation, emission and latent heat flux in fact drive the surface temperature to the wet adiabat, which is the expression of vapor pressure equilibrium in the presence of a vertical pressure gradient. Thus the timescale for depositing 1 km of N_2 ice in the Sputnik Planitia basin is of order 1 Ma (Trafton and Stansberry, 2015), while the time to deposit several kilometers is 10 to 30 Ma because the rate of infilling is proportional to the ever-decreasing depth as the basin is filled (Bertrand and Forget, 2016). However, once formed, such a large deposit has an important influence on the global energy balance of Pluto's N_2 ice. On shorter timescales, seasonal transport can locally sublimate or deposit approximately 1-meter thick layers of N_2 ice over a Pluto year.

The competing influences of seasonal and longer-term topographic volatile transport are apparent in the distribution of Pluto's N_2 and other volatile ices, as measured by New Horizons. In Figure 4 we present a histogram of elevation and band depth of the 2.15-μm absorption band of N_2. Here we used only the band depth map to explore the relationship between elevation and N_2 distribution because the band depth includes both grain size and fractional abundance on the spectrum. Had we used the maps of Protopapa et al. (2017), it would have been necessary to consider both grain size and fractional abundance, resulting in 3-D histograms of the topographic distribution. For the CH_4 distribution, we additionally made use of the Protopapa et al. (2017) N_2:CH_4 dilution ratio map. Figure 4 suggests that there are two main reservoirs of N_2 ice on Pluto: Sputnik Planitia (at an elevation around -3 km and with the strongest band strengths), and the rest of the planet, with N_2 occurring at 0 km elevation and in deep craters, indicative of topographic-driven transport. In terms of area, Sputnik Planitia represents a fairly small fraction of the N_2 ice on Pluto, but the strength of the 2.15-μm band is systematically stronger there than in other regions. The more widely distributed N_2 at higher elevations has weak absorption strengths, and is predominantly in areas with high CH_4 abundance (as indicated by the N_2 band strength being near zero, see Figure 18 of Schmitt et al. (2017)).

Methane also participates in volatile transport on Pluto, albeit not as a primary constituent of the atmosphere (Hinson et al., 2017; Young et al., 2017). Figure 5 is the 2-D histogram of elevation vs. CH_4 band depth. Here we rely on the Schmitt et al. (2017) CH_4 maps shown in their Figure 13. Unlike the N_2 band depths shown in Figure 2, the detections of CH_4 are robust across Pluto's surface. The distribution reveals something of a dichotomy, as does that of N_2. Sputnik Planitia produces a significant cluster of pixels with strong absorption at an elevation of -3 km, and a second, larger cluster with (in some cases) weaker absorption occurring near 0 km elevation. However, CH_4 also occurs at higher elevations than N_2 directly detected via the 2.15-μm absorption feature, and at higher elevations (up to nearly 2 km) the bands are just as strong as those in Sputnik. As shown in the lower panel of Figure 5, CH_4 diluted in N_2 is mostly concentrated at low elevations.

Figure 6 shows the elevation distribution of CO ice, based on the Schmitt et al. (2017) band depth measurements from very high spectral resolution measurements. Merlin *et al.* (2018) conclude that the width of the CO absorption bands on Triton imply that the CO there is present *only* dissolved in N_2 ice. If that were true on Pluto, the CO absorption

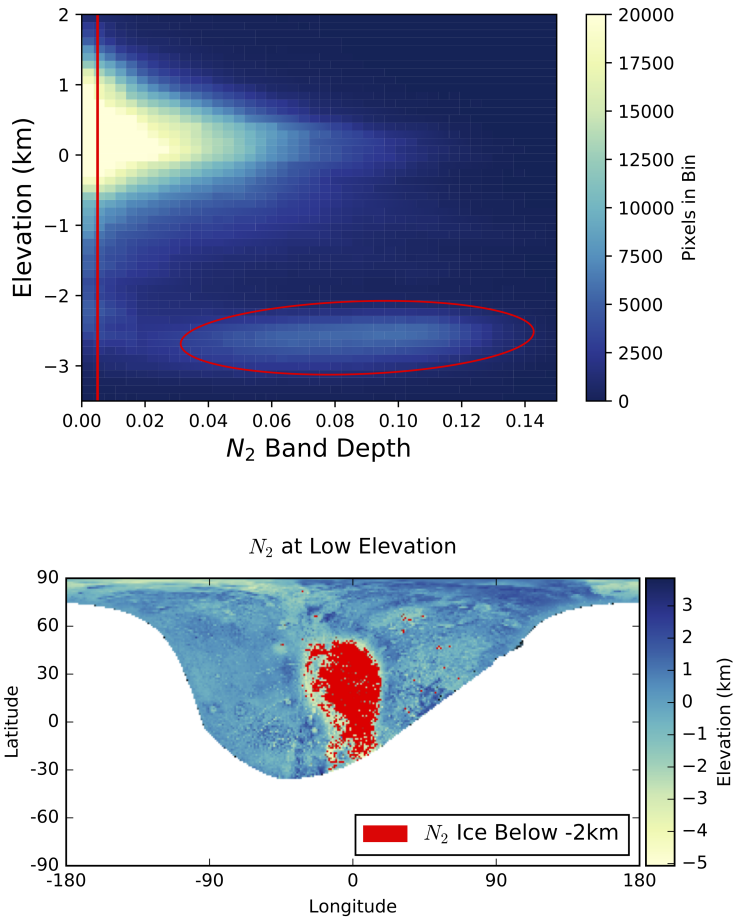

Figure 4: Histogram of integrated nitrogen band depth (Schmitt et al., 2017) vs. elevation (top). The significant clump of strong N_2 absorption at elevations near -3 km is mostly due to N_2 ice in Sputnik Planitia (map of points in this region of parameter space shown on bottom panel, circled on top panel). A second band of N_2 occurs near 0 km, but does not extend to the strongest absorption strengths seen in Sputnik. Band depth values less than 0.005 (as indicated by the vertical red line, top) are spurious.

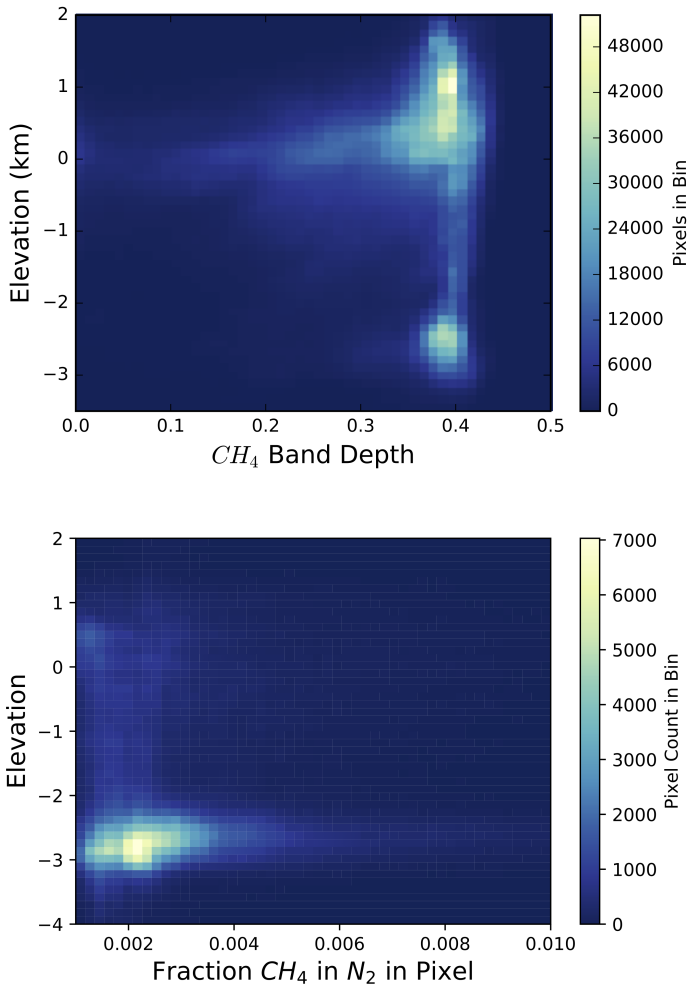

Figure 5: Top: 2-D histogram of integrated methane band depths (Schmitt et al., 2017) vs. elevation. The clump of pixels at -3 km elevation maps to Sputnik Planitia. Bottom: 2-D histogram of CH_4 diluted in N_2 vs. elevation (Protopapa et al., 2017). Methane present in solution with nitrogen shows clear evidence of downward topographic transport.

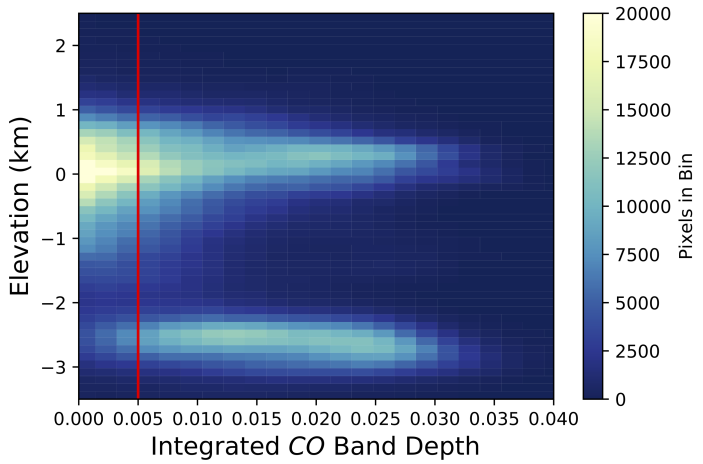

Figure 6: Histogram of integrated carbon monoxide band depth (Schmitt et al., 2017) vs. elevation. The cluster of pixels at -3 km elevation maps to Sputnik Planitia, similar to the N_2 distribution shown in Figure 4. The vertical red line denotes the limit for reliable, physical band depth measurements (0.005).

band maps could be used as a tracer for N_2, just as the binary N_2 map used for this study included the band-shifted CH_4 absorptions as a tracer of N_2. Indeed, the CO ice distribution in Figure 6 closely resembles the N_2 ice distribution in Figure 4, suggesting a close physical association between these molecules on broad spatial scales. This is also a conclusion of Schmitt et al. (2017), which also identified a trend of N_2 with weak or no CO, corresponding to N. Vega Terra, Hayabusa Terra, and Pioneer Terra. Unfortunately measuring or fitting the CO ice band in the LEISA data is difficult. The band depth data lie primarily below the threshold of 0.005, although valid band depths are seen at both -3 km (which we have verified to map to Sputnik Planitia) and near 0 km elevation. Attempts to fit spectral models to that band by Protopapa et al. (2017) were frustrated by the lack of adequate optical constants in the wings of the band, and no results for CO were presented there. Thus, while the similarities between the elevation distributions of CO and N_2 on Pluto are suggestive, CO ice is even harder to detect in the LEISA spectral band than is N_2 ice making it impractical to use as an additional "tracer" for N_2.

In summary, the figures above show that large-scale topography on Pluto does indeed influence the distribution of N_2, CH_4 and CO. Nitrogen ice in Sputnik Planitia basin, with both CH_4 and CO dissolved in it, is evidence of the slow but steady down-hill transport of those ices caused by the atmospheric pressure gradient, and is not expected to be significantly disturbed by seasonal redistribution of the ices (Bertrand and Forget (2016)). (Below we discuss the distribution of sublimation and condensation of N_2 within Sputnik Planitia at the time of the New Horizons encounter.) Outside Sputnik Planitia, at least on the encounter hemisphere, the N_2 ice is distributed approximately in latitude bands that are consistent with expected seasonal transport (*e.g.* Young (2013)), with albedo and topography (*e.g.* altitude) of the surface modifying the distribution within latitude bands. In other words, lower albedo regions in a given latitude band tend to

have less N_2 than the higher albedo regions. We explore further the albedo of the N_2 ice in the following section.

2.3. Total Nitrogen Ice Inventory

Using these maps and observations, it is possible to put a lower limit on the total amount of N_2 on Pluto. By multiplying the fractional abundance, pixel area, and equating the grain sizes from Protopapa et al. (2017) to the local depth of the N_2 ice (a severe lower limit on the layer depth due to the transparency of the N_2), and integrating over the map, we derive a lower estimate of the volume of N_2. Grain size values that correspond to a N_2 abundance less than 10% are invalid, so these were excluded from the calculation (as stated in Protopapa et al. (2017)). For reference, typical N_2-ice grain sizes were found to be $\simeq 50$ cm by Protopapa et al. (2017). Note that this calculation did not include the extrapolated fractional coverage beyond the encounter hemisphere, since we were interested in a lower limit based only on the available data. Through this method, we found that there is approximately $6 * 10^2$ km^3 of N_2-ice distributed across the globe outside of Sputnik Planitia. The total amount of N_2 on Pluto has implications for understanding how N_2 was incorporated during the formation of Pluto, as investigated in Lisse et al. (2019).

Is SP the dominant reservoir of N_2, or a relatively equal contributor compared to the rest of the surface? Given that the N_2 ice layer in Sputnik Planitia is estimated to be kilometers thick (McKinnon et al., 2017), so the grain sizes are not appropriate for estimating the N_2 inventory there. Instead we integrated over the area of the Sputnik basin, assuming a uniform composition of pure N_2 and a depth of 3 km. This resulted in approximately 3.5×10^5 km^3 of N_2 in SP alone. That is 500 times more than the lower bound calculated above for the N_2-ice inventory outside SP Given that the N_2 ice outside SP generally does not tend to mute, let alone obscure, underlying topography, it seems unlikely that its typical depth would be 500 times greater than assumed above (*i.e.*250 m on average). Thus SP likely represents the largest reservoir by volume of N_2 ice on Pluto by far. As such, it isn't surprising that we see evidence of SP playing a key role Pluto's atmospheric cycles (Bertrand et al., 2018).

3. Energy balance and transport of Pluto's N_2 ice

Using the map of N_2 ice distribution described in Section 2, we examined the global energy balance of the ice. Because the atmosphere is supported via vapor pressure equilibrium with the global N_2 ice inventory, its energy balance is a key consideration for understanding the overall surface-atmosphere system, and provides insights into processes governing the redistribution of N_2 (and other volatile ices) on seasonal and climatic timescales. As mentioned in Section 1 (and based on the extensive discussion in Trafton and Stansberry (2015)), the expected non-ideal vapor pressure behavior of N_2:CH_4 ice might have significant implications for both latent heat redistribution and the link between the temperature of the N_2 ice and the atmospheric pressure. Lacking any laboratory constraints on those non-ideal effects, we assume for now that the solid solution ice N_2:CH_4 (N_2-dominant mixture) behaves like pure N_2 ice.

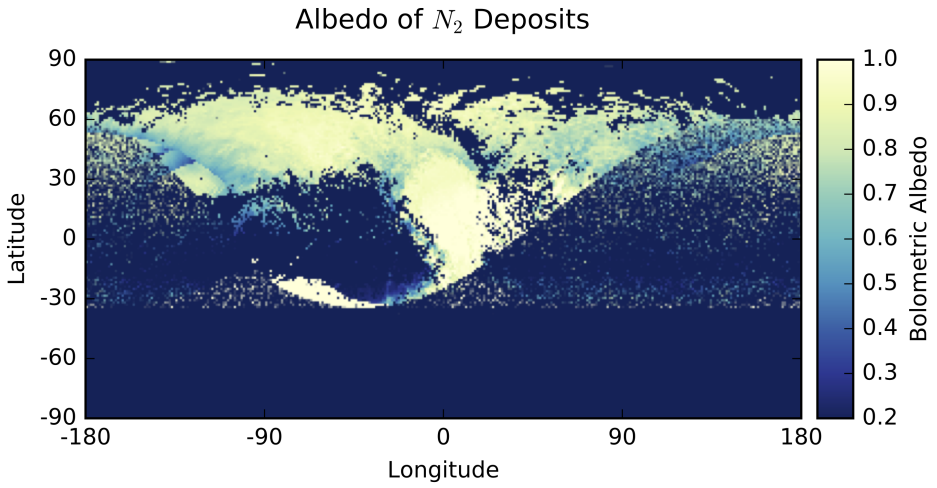

Figure 7: Map of bolometric albedo (Buratti et al., 2017) of nitrogen deposits across the surface. Areas lacking LORRI data, and therefore albedo determinations, but north of -38° latitude are filled in in the same manner as for the N_2 presence map of 2, using the average albedo of N_2 in all other areas.

3.1. Bolometric albedo, temperature, and emissivity of the N_2 ice

Maps of bolometric albedo, determined from LORRI data, over a bandpass of $0.61 \pm 0.2\,\mu$m (Buratti et al., 2017), were combined with the global map of nitrogen presence from Section 2.1 to create a map of the albedo of nitrogen deposits across Pluto's surface, as shown in Figure 7. These albedos are somewhat approximate, as described in Buratti et al. (2017). A full analysis of the spatially-dependent phase function of Pluto has not yet been done, so the bolometric albedos shown here are based on the Triton phase function (Hillier et al., 1990). While this approach may result in some inaccuracies, Buratti et al. (2017) show that Pluto's and Triton's phase functions at the global scale are very similar. Thus, the resulting errors in our calculations of absorbed insolation and energy balance of the N_2 ice are small in the globally-averaged sense. Hillier et al. (1994) examined the photometric properties of various terrains on Triton, finding that the bolometric albedos for those terrains likely to be associated with N_2 ice differed by no more than about 10% from the global bolometric albedos in their 1990 study.

Pluto's N_2 ice will also absorb insolation at near-IR wavelengths, due primarily to the few percent of CH_4 dissolved in it. We estimated the magnitude of this effect using the global-average spectrum of Pluto from 0.7 – 5.0 μm. We assumed that the N_2 ice is spectrally neutral below 0.7 μm, and normalized the entire spectrum to an albedo of 0.62 at 0.7 μm. The integral of the product of that spectrum and the solar spectrum was 1.09 times the integral assuming a constant albedo of 0.62 over the entire range. Because it is the dissolved CH_4 that must be responsible for the bulk of that additional absorption in this calculation, and the CH_4 band strengths in the N_2:CH_4 solid solution may be weaker than for the global-average spectrum (because N_2, and not CH_4, is the dominant species in those ices), the estimate above may be an upper limit on the additional insolation absorbed by Pluto's N_2 ice in the near-IR.

With the bolometric albedo map, we can now compute the globally averaged energy balance of the N_2 ice. As discussed earlier, latent heat transport through the atmosphere maintains all of the N_2 ice at a single temperature (T_{N_2}), and the heat content of Pluto's thin atmosphere is negligible, so the globally averaged energy balance is the prime consideration for computing T_{N_2}. Equation 1 equates the total thermal radiation from the N_2 ice to the total insolation absorbed by the ice. We assumed that the emissivity was the same for all the N_2 ice (with an assumed value of unity), and used the solar flux at Pluto's distance (S_0) appropriate for July 2015 (the time of flyby) from the JPL HORIZONS ephemeris database. The bolometric albedo of the ice (A_{N_2}), was taken from Figure 7.

$$\epsilon_{N_2} \sigma T_{N_2}^4 \int_{N_2} dA = S_0 \int_{N_2} (1 - A_{N_2}) < \cos\mu > \, dA \tag{1}$$

The integrals were carried out over the entire surface (left-hand side), and over the lit fraction of the surface (right-hand side), where N_2 ice was present (Figure 2). A further simplification was possible because the time scale to change Pluto's atmospheric mass is much longer than Pluto's day, so we used the diurnal average ($< \cos\mu >$) of the insolation angle at each latitude. The terminator longitude at each latitude is given by Equation 2, where β_T is the angle from the sub-solar meridian to the terminator, θ is the co-latitude and θ_S is the co-latitude of the subsolar point.

$$\cos\beta_T = \frac{-1}{\tan\theta\tan\theta_s} \quad (2)$$

Figure 8 shows the pattern of diurnally averaged incident and absorbed solar flux for Pluto's N_2 ice. The flux incident on the N_2 ice is dominated by the subsolar latitude (51.6°N) at the time of the encounter and the overall presence (and absence) of N_2 ice. The absorbed insolation is much smaller, illustrating the strong modification of the insolation by the high albedo of the N_2 ice.

We solved Equation 1 for T_{N_2}, and present the implications of the result below. While there are no data constraining the presence of N_2 ice in the *terra incognita* (*i.e.* un-illuminated portions of Pluto, below 38°S), N_2 ice present in that area significantly affected our results for T_{N_2}. In the absence of observations of the *terra incognita* region, we adopted 5 possible distributions for the N_2 ice there: 1) no N_2, 2) minimum longitudinal-average coverage, 3) mean longitudinal-average coverage, 4) maximum longitudinal-average coverage, and 5) completely covered in N_2 ice. (See Figure 2 for the longitudinal average values, and Figure 12 for realizations of cases 2 through 4.) The details of the distribution of the N_2 ice within the un-illuminated areas is unimportant for the global energy balance: only its contribution to the area on the left-hand side of Equation 1 matters.

Models of long-term seasonal transport on Pluto combined with the history of atmospheric pressure established by stellar occultations can predict the distribution of the N_2 ice in the *terra incognita*, but are subject to significant uncertainties in model parameters and assumptions (in particular thermal inertia and total N_2 ice inventory). Model results presented by Young (2013), Bertrand and Forget (2016) and Bertrand et al. (2018) tend to favor fairly high thermal inertia (800 – 3000 $\mathrm{J\,m^{-2}\,s^{-1/2}\,K^{-1}}$, about 0.3 to 1 times that of solid H_2O-ice) because they better match the sustained increase in Pluto's atmospheric pressure observed between 1989 and now. Those model cases predict little or no N_2 ice in the far south at the time of the New Horizons encounter. However, some model runs in Young (2013) (particularly a few of the "exchange with pressure plateau" runs) result in some N_2 ice south of -38°. Forget et al. (2017) and Bertrand and Forget (2017) present GCM models for Pluto's atmosphere in 2015 and find that the presence of some N_2 ice in the far south may be more consistent with the inferred meridional circulation of Pluto's atmosphere. Thus, while seasonal transport modeling can, subject to uncertainties in several model parameters, predict the distribution of N_2 ice in the *terra incognita*, at this time the range of model predictions does not strongly constrain it. We note that the unknown altitude of terrains south of -38° could have a controlling influence on the distribution of N_2 ice there: a large basin would, like SP, be filled with N_2 while if that region is systematically higher than Z_{N_2} it would be less prone to condensation of N_2. The cases outlined above span this range of possibilities, but in the absence of any actual constraints on the overall topography in the *terra incognita* we don't assume a strong influence by topography there.

Figure 9 shows the results of our energy balance calculations for Pluto's N_2 ice. The 5 assumed configurations of N_2 ice in the un-illuminated regions in the south are plotted as symbols, with the value of T_{N_2} for each configuration on the x-axis. For each model, we calculated the bolometric emissivity of the N_2 ice required to give $T_{N_2} = 36.93\,\mathrm{K}$, (the emissivity was assumed to be the same for all of the N_2 ice). These results, like the GCM and seasonal models summarized above, suggest that significant deposits of N_2 ice

in the southern *terra incognita* region are unlikely. For cases 5 ('all-N_2') and 4 ('high-N_2'), the bolometric emissivity would be 0.32 to 0.46, straining the bounds of plausible emissivities. For our case 3 ('average N_2'), the range is 0.53 to 0.65, while for cases 2 and 1 ('low-N_2' and 'no-N_2'), the range is 0.70 to 0.86. These ranges include an assumed 10% assumed systematic uncertainty on the emissivity, consistent with likely uncertainties in the bolometric albedos and the accuracy of our N_2 ice occurrence map. Based on the GCM and volatile transport modeles discussed above, it seems most probable that there is some N_2 ice in the *terra incognita*, perhaps consistent with our case 3. If we include the upper emissivity bound for high-N_2 case (4), and the lower emissivity bound for the low-N_2 case (2), we adopt a plausible range of emissivities $0.47 < \epsilon < 0.72$ based on these results.

It is unclear which of these cases best represents Pluto's real N_2-ice distribution in the south, but the results strongly suggest that Pluto's N_2 ice has a bolometric emissivity below unity, with quite low values allowed. This is similar to conclusions drawn by Stansberry et al. (1992) regarding Triton's N_2 ice, although we are arguably on much firmer footing regarding Pluto's energy balance because the LEISA spectra show where the N_2 is on the surface (no such data were available from Voyager 2 for Triton). It is also consistent with preliminary results from the New Horizons REX radiometric measurements of the brightness temperature of Pluto's surface, which suggest that the directional, 4.2-cm emissivity (*i.e.* non-bolometric) in Sputnik Planitia is approximately 0.7 (Linscott *et al.*, *submitted*). It is important to note, though, that the REX radiometric measurements were made at a very different wavelength from where the bulk of thermal emission happens.

4. Discussion

We derived a map of the distribution of N_2 ice on Pluto utilizing the LEISA spectra of the encounter hemisphere, merging lines of spectroscopic evidence from the encounter hemisphere and extrapolating the latitudinal N_2 distribution there to other longitudes, to try and provide as realistic a map as possible. The resulting energy balance on Pluto's N_2 ice suggests that the bolometric emissivity is likely in the range 0.4 – 0.8, which is consistent with the range of estimated values for Triton based on a similar analysis (Stansberry et al., 1992). Below, we discuss the statistical nature of the N_2 ice bolometric albedo, useful as an input to seasonal/climate models, and explore implications for the state of volatile transport on Pluto at the New Horizons epoch, and for the fate of Pluto's atmosphere at larger heliocentric distances.

4.1. Latitudinal albedo trends

To further investigate the bolometric albedo of Pluto's N_2 ice, we binned the albedo map (Figure 7) into sections of 1 degree of latitude. We then computed the average, root-mean-square (RMS) deviation, and minimum albedo of the N_2 ice only (Figure 2) in each latitude bin, as shown in Figure 10. At latitudes north of $+20°$, the N_2 ice albedo is relatively constant at about 0.8, with an RMS scatter of about 0.1. The albedo is slightly higher ($\simeq 0.85$) near $+30°$ due to the very high albedo deposits in Sputnik Planitia. Albedo is also slightly higher above $+70°$, but there is relatively little N_2 ice there in terms of the total area in that region or in terms of the fractional coverage (see

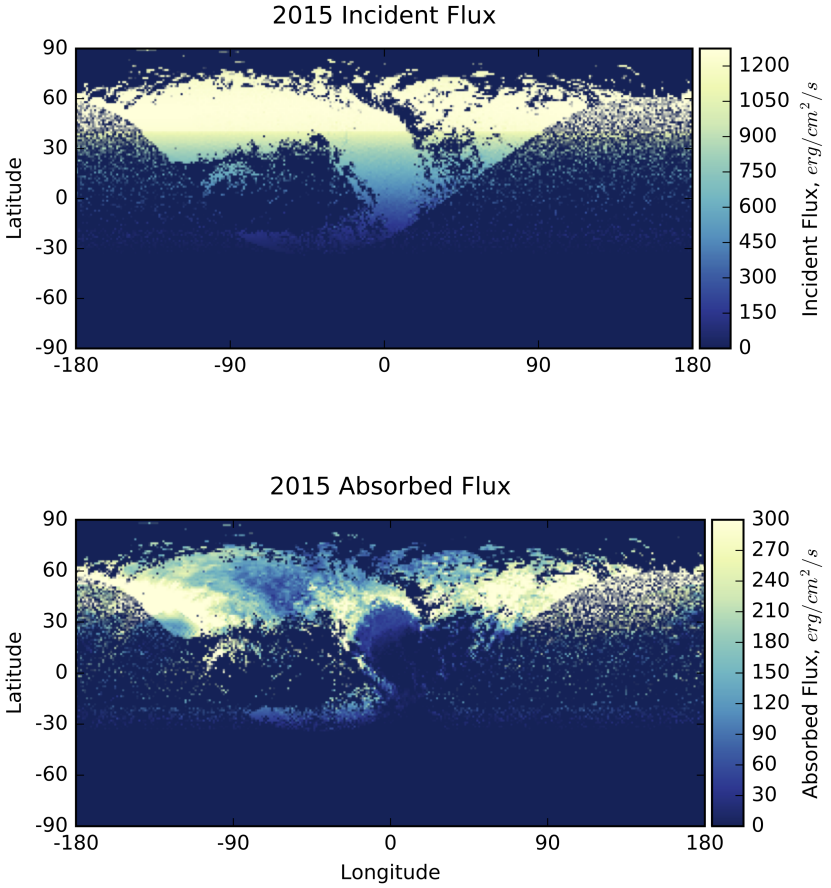

Figure 8: (Top) Diurnally-averaged incident solar flux ($< S_0 >$) at the time of the New Horizons flyby, for areas we have identified as having N_2 ice. (Bottom) Absorbed solar flux at the time of the flyby, as given by $< S_0 > (1 - A)$, where A is the bolometric albedo (Figure 7).

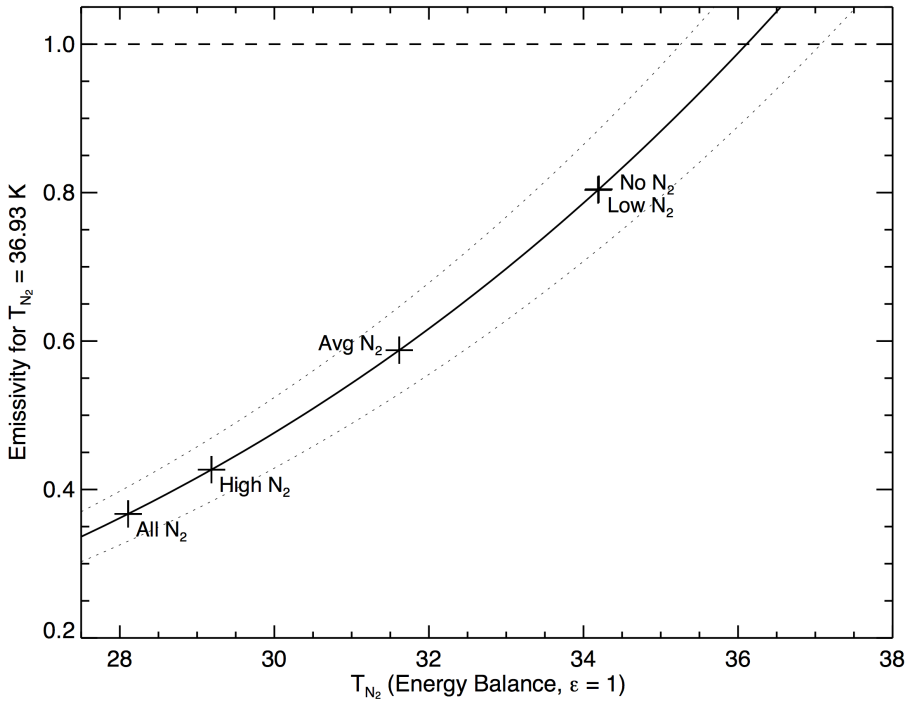

Figure 9: Bolometric emissivity of Pluto's N_2 ice required to match the temperature ($T_{N_2} = 36.93K$) inferred from the atmospheric pressure of 11.5 μbar (solid line). Results of our energy balance calculations (which assumed emissivity = 1) are overplotted as crosses, with labels indicating the 5 cases of assumed distribution of N_2 ice in the un-illuminated regions south of -38° latitude. Dotted lines indicate an assumed systematic uncertainty of 10% on the emissivity we derive, while the horizontal dashed line at an emissivity of unity marks the physical upper limit.

Figure 2). The average bolometric albedo of the N_2 ice near Pluto's equator falls to about 0.65, rising again to about 0.8 at the southern limit of the data. The N_2 albedo minimum near the equator, and the lowest N_2 ice albedos at each latitude (Fig. 10), could result from pixels covering a patchwork of N_2 ice and low albedo bare areas, a relatively transparent layer of N_2 overlying low albedo substrate, or a combination of the two.

Areal mixing seems the more likely explanation for the apparently low N_2 ice bolometric albedos near Pluto's equator (and the minimum albedos at all latitudes). The equator was strongly illuminated recently, in the years near equinox (1987), and low-albedo areas would have warmed significantly. Those warm surfaces would be unlikely to become sites of N_2 condensation, particularly for enough condensation to yield a measurable N_2 spectral feature. If the low equatorial albedos are indeed the result of areal mixing of N_2 and bare regions, then the actual albedo of N_2 ice itself near the equator could be much higher than indicated in Figure 10, and could easily be around 0.8, as it is further north and south. Further, this would imply that our energy balance calculations presented earlier somewhat overestimate the amount of insolation absorbed by the N_2 ice. In turn that implies that the actual emissivity of the N_2 ice would be somewhat lower than illustrated in Figure 9. As can be seen in Figures 2 and 7, the amount of low-albedo N_2 near the equator is relatively small compared to the total inventory, so the overestimate of T_{N_2} and N_2 emissivity resulting from areal mixing of N_2 ice and low albedo materials near the equator should be small.

The average N_2 ice bolometric albedo (and emissivity) on Pluto is of interest for climate and seasonal models. We find that the area-weighted average albedo, and RMS deviation, are 0.78 and 0.16, respectively. As can be seen in 7 and 10, there is a strong correlation between albedo and the presence of N_2 ice. In particular, in 10 the average albedo of the N_2 is greater than 0.6 at all latitudes, and the RMS scatter of its albedo is about 0.1. There is a low-albedo tail to the albedo distribution of the N_2 ice, but given the observations above, it seems likely that the tail is caused by mixing between N_2-ice and dark, N_2-free areas at the sub-pixel scale of the LEISA maps. To correct for the possibility such sub-pixel mixing we exclude some data as follows. Excluding the N_2 albedo data from -20°– +20° latitude, the average and RMS deviation are 0.79 and 0.14, respectively. Excluding albedos less than 0.6 at all latitudes, the average and RMS deviation are 0.83 (6% larger than the global average given above) and 0.11, respectively. We note that the low-albedo tail for N_2 ice in some areas will bias calculations of the energy balance somewhat (*i.e.* to higher emissivities), but because they tend to occur for relatively few pixels, and mostly in areas with moderate to low insolation, that bias will be relatively small.

4.2. Volatile Transport

As described in several previous studies (*e.g.* Stern et al. 1988; Hansen and Paige 1996; Spencer et al. 1997; Young 2013) Pluto's N_2 (and other volatile) ices are constantly being transported across the surface in response to surpluses and deficits of insolation, carrying energy (as well as mass) away from high-insolation regions to low-insolation regions. Figure 11 illustrates the terms in the energy balance near Pluto's surface, including terms for insolation, re-radiation, sublimation/condensation, and subsurface conduction and heat capacity. For calculating the net effect of volatile transport on the distribution of N_2 ice over seasonal and climatic timescales, the conduction and heat-capacity terms are very

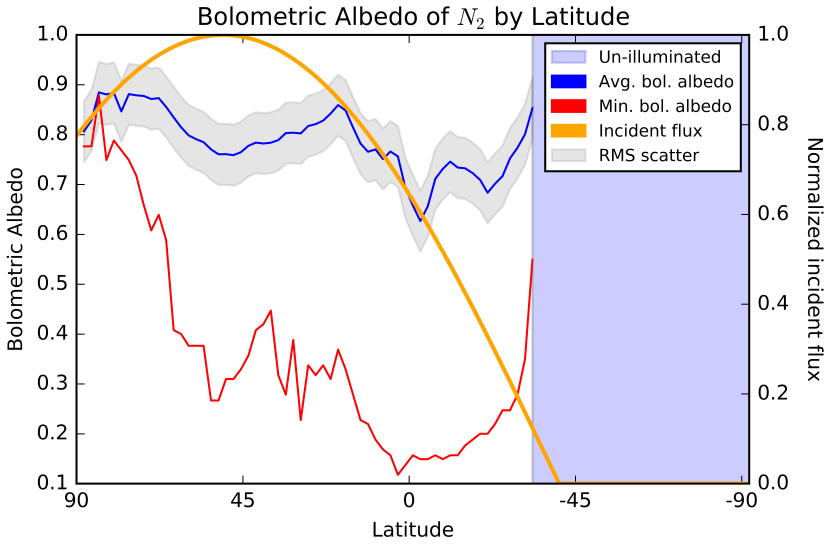

Figure 10: Here we trace the average bolometric albedo of areas containing nitrogen for each latitude on Pluto. This line plot traces the variations in average albedo (blue), the RMS deviation about that average (gray shading), and the minimum albedo of the N_2 ice at each latitude. The diurnally-averaged incident flux is also shown (orange), as calculated in Section 3. The blue region at right represents the un-illuminated section of Pluto at the time of the New Horizons encounter.

important, inducing a time-lag between the insolation cycle (driven by Pluto's obliquity and orbital eccentricity) and temperature variations and sublimation/condensation at the surface.

Our results were extended to provide a snapshot of the rates of sublimation and condensation of N_2 ice at the time of the New Horizons encounter. For this investigation, we ignored the conduction and heat-capacity effects illustrated in Figure 11. Including those effects would have been outside the scope of this work. Under the usual forward-modeling approach, this would have required an historical volatile ice distribution that would evolve, in a seasonal-transport model calculation, to match the observed distribution (and albedo patterns) described in Sections 2.1 and 3.1. An alternative could be to take the N_2 ice distribution we have derived, run a seasonal transport model backward in time, and seek values of the heat capacity and conductivity of the subsurface that matched historical constraints on the volatile distribution (*e.g.* secular trends in atmospheric pressure, and/or the photometric and spectroscopic lightcurves). Either approach would be iterative, rely on oversimplified assumptions about the nature of Pluto's subsurface, be computationally expensive, and would not be guaranteed to provide a result that closely matches our N_2 ice distribution.

In light of the above difficulties of using a full time-dependent volatile transport model to interpret our N_2 ice distribution, we simplified the problem and considered the instantaneous state of volatile transport. Equation 3 gives the simplified form, neglecting the subsurface conduction and heat-capacity terms. Here L is the latent heat of sublimation (2.52×10^9 erg/g), $\frac{dm}{dt}$ is the condensation mass flux, and the other terms are as

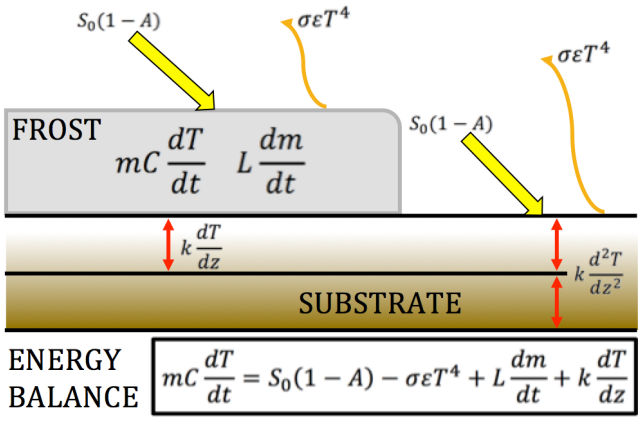

Figure 11: Visualization of energy balance on an icy surface in the presence of insolation ($S_0(1-A)$), thermal radiation ($\epsilon\sigma T^4$), subsurface conduction (kdT/dz) and heat-capacity ($mC_p dT/dt$) and volatile transport (Ldm/dt). Figure adapted from Hansen and Paige (1996).

in Equation 1. To solve this equation for the local mass flux, we set T_{N_2} to 37.2 K, consistent with the atmospheric pressure, and assume $\epsilon_{N_2} = 0.8$, based on our results above and consistent with the emissivity of Triton's N_2 ice (Stansberry et al., 1992). By assuming that T_{N_2} is a constant across Pluto's surface, we are implicitly requiring that the integral of the mass flux over all of the N_2 ice is zero (*i.e.* there is no net gain or loss of N_2 mass due to the transport). In the results presented below we verified that the net calculated mass flux (*e.g.* volatile inventory lost to the atmosphere) is very close to zero ($< 1 \times 10^{-11}$ g/cm^2/pixel). Elevation-driven transport rates (Trafton and Stansberry (2015)) are tiny relative to the insolation-driven rates on this timescale, and so were not included in these calculations.

$$-L\frac{dm}{dt} = S_0(1-A)\cos\mu - \epsilon_{N_2}\sigma T_{N_2}^4 \tag{3}$$

The resulting mass fluxes of subliming and condensing nitrogen are shown in Figure 12. As mentioned in Section 3.1, the energy balance at the surface depends on the amount of N_2 ice present south of -38° latitude, where there is no data. Also mentioned earlier, we considered 5 cases spanning the range of possible N_2 coverage there, ranging from no-N_2 to covered in N_2 (see description of the cases in the discussion of Figure 9). Three of those cases (representing coverage at the minimum, average, and maximum longitudinally-averaged coverage from Figure 2) are represented in Figure 12. The patterns of condensation (positive mass fluxes) and sublimation are rather similar for all three cases shown. In general, there is transport from the higher-insolation areas in the north towards the south. Sputnik Planitia is, on average, experiencing condensation of N_2 ice, except in the northernmost areas (we return to this topic below). The low-albedo N_2 ice in western Cthulhu Regio is predicted to be actively sublimating (but this may not actually be the case if the N_2 ice actually has a fairly high albedo and is segregated at the sub-pixel scale from even lower albedo Cthulhu-like material, as discussed earlier).

According to Bertrand et al. (2018), SP is currently at its minimum ice coverage in a sublimation-dominated epoch, so the sublimation we observe at the edges is expected. Their modeling work also suggests that the latitudinal band of N_2 around 30°N is relatively stable, and may be explained by CH_4-rich deposits contributing to a high albedo in that region.

For the low-N_2 coverage case (top panel) the N_2 condensation fluxes are significantly larger than for the average- and high-coverage cases (lower panels). This is because N_2 ice is not present (and so is assumed unable to undergo condensation) in the un-illuminated area, and all of the mass sublimated in the illuminated region must also condense there. The calculated sublimation/condensation limit (where mass flux is 0) is 38.34°N, as shown in Figure 12. Because we are assuming the same surface pressure for all models, the location of the sublimation/condensation limit is independent of the assumed N_2-ice distribution in the un-illuminated regions. Instead, the magnitude of the sublimation rate changes to account for the changes in areas where condensation occurs.

The situations for the average- and high-N_2 coverage cases (Figure 12, lower panels) are less likely to represent the volatile transport that was occurring at the encounter epoch. Of particular interest is the transition between sublimation and condensation within Sputnik Planitia basin. These results suggest that the northern-most part and the north-west border were undergoing weak sublimation, while condensation dominated over the larger southern area of Sputnik. The location of the sublimation/condensation transition agrees well with a contrast in the grain size of, and CH_4 concentration in the N_2:CH_4 component in the composition maps of Protopapa et al. (2017) and Earle et al. (2018), Figure 5. Our sublimating area correlates with their region (local to Sputnik) of smaller grain size and higher CH_4 concentration in the N_2 ice. The CH_4 concentration correlation seems to be consistent with the preferential removal of N_2 via sublimation of N_2:CH_4 ice, as was suggested by Stansberry et al. (1996b). The fact that the sublimation of N_2:CH_4 seems to be correlated with smaller grain sizes for that component in northern Sputnik could be due to the surface becoming rougher, or grain boundaries widening, as sublimation proceeds, resulting in a more highly scattering material. However, an increase in scattering seems inconsistent with the slight albedo contrast between northern and mid- to southern Sputnik: bolometric albedo in our region of sublimation is $\simeq 0.94$, and is $\simeq 0.98$ further south in Sputnik. A similar gradient in normal reflectance is also seen (Buratti et al., 2017). This apparent discrepancy could be the result of the smaller grains being more forward scattering (and thus yielding a lower albedo in back-scatter) than the grains being formed further south, or (more likely) the concentration of lower-albedo contaminants in the N_2 ice (*e.g.* haze particles) as the ice sublimates.

4.3. The fate of Pluto's atmosphere

Stansberry et al. (1996b) explored the implications for low N_2 ice emissivity for seasonal changes in Pluto's atmosphere. Specifically, they show that if there is an emissivity contrast between the solid α and β phases of nitrogen, with the emissivity of N_2^α being lower, Pluto's atmospheric pressure would plateau at $4.8\,\mu$bar, the vapor pressure at the $\alpha - \beta$ transition temperature (35.6 K, Fray and Schmitt (2009)). Hapke theory calculations of the bolometric emissivity of both phases of N_2 (Stansberry et al., 1996a) show that N_2^α should in fact have a lower emissivity, with the emissivity contrast with N_2^β being largest near the $\alpha - \beta$ transition temperature. The magnitude of the emissivity

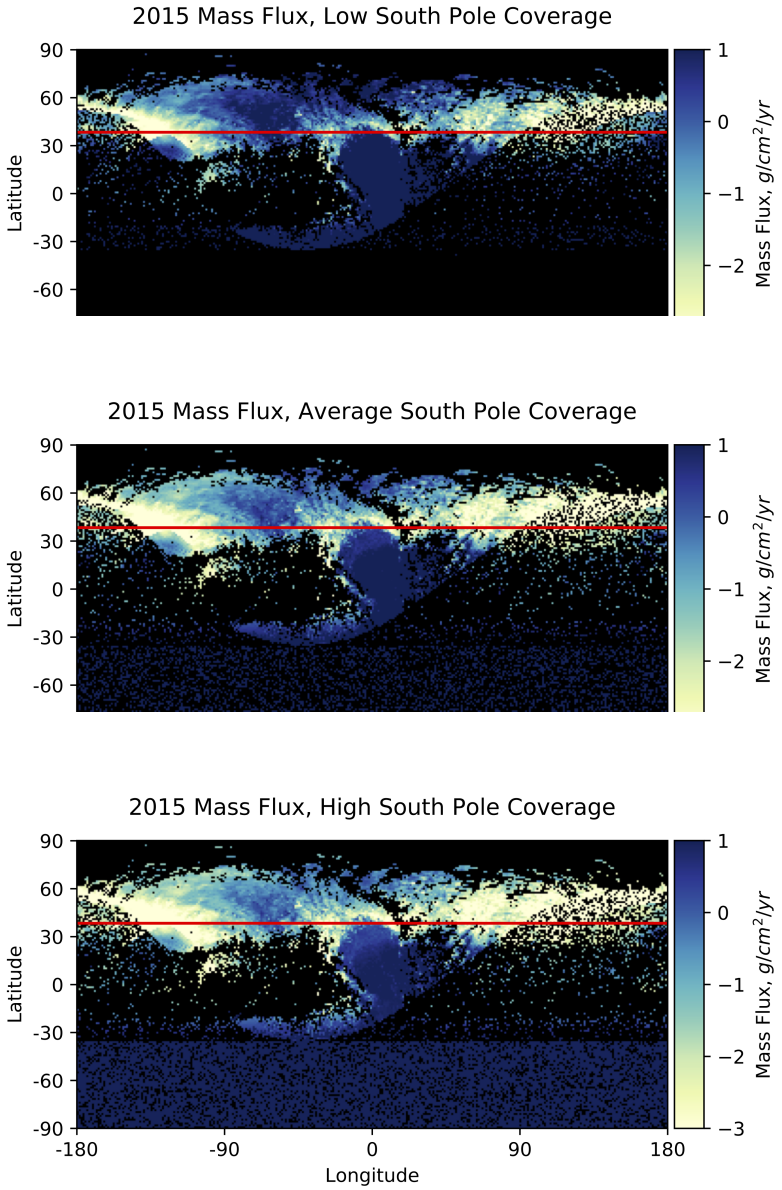

Figure 12: Mass fluxes of N_2 ice condensation (positive) and sublimation (negative) based on our N_2 ice distribution and energy balance calculations (Equation 3). Red lines indicate the longitudinally-averaged sublimation/condensation boundary, *i.e.* on average sublimation is occurring north of the line, and condensation to the south. Three cases are shown from the 5 we considered for the N_2 ice distribution in the un-illuminated regions south of -38°. (Top) N_2 ice coverage at the minimum value we derive for the encounter hemisphere; (Middle) coverage at the average encounter-hemisphere value; (Bottom) coverage at the maximum encounter-hemisphere value. The other two cases are no N_2 ice coverage below -38° (which is very close to the minimum coverage case shown in the top panel, see Figure 9), and completely covered in N_2. Details of the distribution of the N_2 in the un-illuminated area are irrelevant for the mass fluxes; we illustrate them using random selection of pixels with the appropriate fractional coverage (note blue speckles).

contrast is grain size dependent, but as long as the phase transition from N_2^α to N_2^β does not spontaneously result in much larger grains of N_2^α, the contrast should be significant (a factor of $\simeq 3$ is typical in their calculations). The fact that N_2^α is slightly more dense than N_2^β also suggests that as N_2^α forms from N_2^β due to cooling, effective grain sizes may become smaller, *e.g.* as grain boundaries open. The emissivity calculations neglected possible effects of CH_4 and/or CO dissolved in the N_2 ice. Either of those contaminants would raise the emissivity of the N_2 because of their stronger far-IR absorption features. These contaminants also alter the transition temperature: CH_4 lowers it, while CO raises it. Qualitatively, the effect of CH_4 or CO dissolved in the N_2 could be offset by assuming a reduced N_2 grain size.

Our results here suggest that the emissivity of N_2^β (the phase expected for $T_{N_2} > 35.6\,K$) on Pluto is indeed low. From the results in Stansberry et al. (1996a), the emissivity is consistent with effective grain sizes (for emitted wavelengths near $100\,\mu m$) of order 0.5 cm, assuming pure N_2 ice. The presence of CH_4 diluted in the N_2 ice will result in somewhat higher emissivity, so the effective grain size required to match our emissivity estimates would be somewhat smaller. At a grain size of 0.5 cm, the emissivity of N_2^α is expected to be a factor of 5 lower than for N_2^β. As Pluto recedes from the Sun its N_2 ice will cool to the $\alpha - \beta$ transition temperature, and N_2^α will begin to form. As that happens the effective globally averaged emissivity of the N_2 ice will drop, causing its equilibrium temperature to stall at the phase-transition temperature. This effect could actually be stronger than discussed in Stansberry et al. (1996a) because the phase transition is accompanied by a reduction in volume, which could result in smaller grains and/or stronger scattering at grain boundaries. Further, the solubility of CH_4 is lower in N_2^α than in N_2^β, so if dissolved CH_4 is raising the emissivity relative to the earlier calculations, ex-solution of the CH_4 during the phase change would increase the emissivity contrast between N_2^α and N_2^β.

While not explicitly discussed in Stansberry and Yelle (1999), the simultaneous presence of the two solid phases (N_2^α and N_2^β) in contact with the gas-phase atmosphere locks the N_2-ice/atmosphere system into a state with zero degrees of thermodynamic freedom until one of the phases is exhausted, so the state variables (*e.g.* pressure and temperature) are also unable to change. Thus our finding that Pluto's current N_2-ice emissivity is low suggests that Pluto's atmospheric pressure may experience an extended period of stability at around $4.6\,\mu bar$ in the coming decades as N_2^β converts to lower-emissivity N_2^α .

There could be geologic expressions of the change from N_2^α to N_2^β, although the situation is complex enough that one can only conjecture as to what they might be. It true that the density of N_2^α-ice is slightly higher than that of N_2^β (Scott, 1976); thus the cooling phase transition should result in smaller grains and perhaps larger or additional inter-grain spaces. This might result in an increase of albedo as the α–β phase transition occurs. The N_2^α will also tend to form where the N_2 ice is 'coolest', *e.g.* on the winter hemisphere, nightside, and on topographic highs where the atmospheric pressure gradient favors sublimation over condensation, and the local equilibrium temperature can be slightly lower than the globally-defined T_{N_2}. Detecting N_2^α ice in low- and no-illumination areas seems precluded for the most part, but a spectrometer on a fly-by or orbiting spacecraft, with sufficient sensitivity and resolving power, might be able to detect high-elevation day-side patches of N_2^α, particularly if it included the much stronger

4.3 μm band of N_2.

5. Conclusions

In this work, we created a new map of the N_2 ice distribution on Pluto, synthesized from previously published composition maps of the New Horizons encounter hemisphere, and extrapolated to Pluto's entire surface. Because it is based in part on the detection of bands of CH_4 dissolved in the N_2 ice, this has resulted in a more complete description of the geographic distribution of the N_2 ice than possible using its elusive 2.15- μm absorption feature alone. We used the map to compute the latitudinal and altitude dependent distribution of the N_2, and its average albedo. We then examined the global energy balance of the N_2 ice and used the measured surface pressure to constrain its bolometric emissivity.

We found that global-scale topography is anti-correlated with strong N_2-ice absorption band depths, indicating large grains of that ice particularly in (but not limited to) the huge Sputnik Planitia basin. This was also reported soon after the 2015 encounter (*e.g.* Grundy et al. (2016)), and our new map of the N_2 distribution does not change that conclusion. This confirms pre-encounter predictions of long-term down-hill transport of N_2(*e.g.* Trafton and Stansberry (2015)), and is also predicted by much more complex global circulation models (*e.g.* Bertrand and Forget (2016)). However there are also higher-altitude deposits of N_2 ice in a broad band between 30°N and 60°N latitude, typically at altitudes of 0 to 0.5 km and having generally weaker 2.15- μm band depths than observed in Sputnik. We also provided a lower bound on the total amount of N_2 on Pluto, on the order of 10^5 km^3, illustrating that a large fraction of the nitrogen is contained within Sputnik Planitia.

The latitudinally averaged bolometric albedo of Pluto's N_2 ice ranges from 0.65 to 0.95. Excluding albedos lower than 0.6, which probably result from areal mixing of N_2 and darker materials at the sub-pixel scale, the global average bolometric albedo is 0.83, with an RMS scatter of 0.11, similar to that inferred for Triton. In the case of Pluto, the value is better substantiated because it is based on the actual distribution of the N_2 ice inferred from the LEISA spectral maps, whereas for Triton no such composition maps were available. On the other hand, Triton's photometric function was better constrained than Pluto's.

Pluto's N_2 ice probably has a low emissivity, and the actual value depends on assumed N_2 ice fractional coverage in the un-illuminated areas south of -38°, but is probably in the range 0.47 – 0.72, similar to Triton. These low N_2^β-ice emissivities are consistent with the results of Stansberry et al. (1996a), which predict even lower emissivities for N_2^α. As described in Stansberry and Yelle (1999), once Pluto's N_2 ice reaches the α–β transition temperature of 35.6 K, vapor pressure balance between the two solid phases and Pluto's atmosphere will tend to stabilize the atmospheric pressure at 4.6 μbar until all of the N_2 ice in contact with the atmosphere converts to one form or the other. This effect could result in Pluto having a significant atmosphere even at aphelion, and could be tested in coming decades by using stellar occultations to measure the atmospheric pressure.

Calculated patterns of volatile transport suggest global north-to-south redistribution, with Sputnik being a northward extension of the region of condensation, caused by its high albedo. Within Sputnik, sublimation is probably occurring in the north and northwest, condensation everywhere else, consistent with details of the spectral fits. These re-

sults are also consistent with the post-New Horizons global climate models of Forget et al. (2017). Typical sublimation and deposition rates are approximately 1 $\mathrm{g\,cm^{-2}\,yr^{-1}}$, with sublimation being more geographically concentrated and therefore somewhat stronger. The low emissivity we find for the N_2 ice tends to slightly enhance rates of sublimation, and decrease rates of condensation, relative to what they would be were the emissivity higher.

There are natural extensions of our energy-balance analysis that are currently limited by the available calibrated data products.For example, LEISA maps for the N_2-ice distribution on the non-encounter hemisphere would improve the accuracy of our results, and are being worked on at this time. While the phase function for the N_2-ice dominated areas also introduces a systematic uncertainty in the phase integral used to calculate the bolometric albedo, such an improvement is unlikely given the limited phase-angle coverage available from New Horizons. Over the long term, measurements of Pluto's atmospheric pressure via stellar occultation will test the validity of the prediction that the transition of N_2^{β} to N_2^{α} will result in a stable atmosphere even as Pluto approaches aphelion.

Acknowledgements

The authors would like to thank NASA for supporting the New Horizons project, and the New Horizons team for making this mission and the results of the flyby possible. This work was supported in part by Space Telescope Science Institute, as a part of their 2017 Summer Astronomy Student Program (SASP), and also in part by NASA Solar System Workings grant NNX15AH35G. Calculations and generation of figures made use of the *astropy* and *ISIS3* software packages.

References

References

Bertrand, T., Forget, F., 2016. Observed glacier and volatile distribution on Pluto from atmosphere-topography processes. Nature 540, 86–89.

Bertrand, T., Forget, F., 2017. 3d modeling of organic haze in plutos atmosphere. Icarus 287, 72 – 86. URL: http://www.sciencedirect.com/science/article/pii/S0019103517300477, doi:https://doi.org/10.1016/j.icarus.2017.01.016. special Issue: The Pluto System.

Bertrand, T., Forget, F., Umurhan, O., Grundy, W., Schmitt, B., Protopapa, S., Zangari, A., White, O., Schenk, P., Singer, K., et al., 2018. The nitrogen cycles on pluto over seasonal and astronomical timescales. Icarus 309, 277–296.

Brown, G.N., Ziegler, W.T., 1980. Vapor pressure and heats of vaporization and sublimation of liquids and solids of interest in cryogenics below 1-atm pressure, in: Timmerhaus, K.D., Snyder, H.A. (Eds.), Advances in Cryogenic Engineering. Springer, Boston, pp. 662–670.

Buratti, B., Hofgartner, J., Hicks, M., Weaver, H., Stern, S., Momary, T., Mosher, J., Beyer, R., Verbiscer, A., Zangari, A., et al., 2017. Global albedos of Pluto and Charon from LORRI New Horizons observations. Icarus 287, 207–217.

Cheng, A.F., Weaver, H.A., Conard, S.J., Morgan, M.F., Barnouin-Jha, O., Boldt, J.D., Cooper, K.A., Darlington, E.H., Grey, M.P., Hayes, J.R., Kosakowski, K.E., Magee, T., Rossano, E., Sampath, D., Schlemm, C., Taylor, H.W., 2008. Long-Range Reconnaissance Imager on New Horizons. Space Science Rev. 140, 189–215. arXiv:0709.4278.

Earle, A.M., Binzel, R.P., Young, L.A., Stern, S., Ennico, K., Grundy, W., Olkin, C., Weaver, H., et al., 2017. Long-term surface temperature modeling of Pluto. Icarus 287, 37–46.

Earle, A.M., Grundy, W., Howett, C., Olkin, C., Parker, A.H., Scipioni, F., Binzel, R., Beyer, R.A., Cook, J., Cruikshank, D.P., et al., 2018. Methane distribution on pluto as mapped by the new horizons ralph/mvic instrument. Icarus 314, 195–209.

Elliot, J.L., Dunham, E.W., Bosh, A.S., Slivan, S.M., Young, L.A., Wasserman, L.H., Millis, R.L., 1989. Pluto's atmosphere. Icarus 77, 148–170.

Forget, F., Bertrand, T., Vangvichith, M., Leconte, J., Millour, E., Lellouch, E., 2017. A post-New Horizons Global climate model of Pluto including the N 2, CH 4 and CO cycles. Icarus 287, 54–71.

Fray, N., Schmitt, B., 2009. Sublimation of ices of astrophysical interest: A bibliographic review. Planetary and Space Sci 57, 2053–2080. doi:10.1016/j.pss.2009.09.011.

Grundy, W., Binzel, R., Buratti, B., Cook, J., Cruikshank, D., Dalle Ore, C., Earle, A., Ennico, K., Howett, C., Lunsford, A., et al., 2016. Surface compositions across Pluto and Charon. Science 351, aad9189.

Grundy, W., Young, L., Stansberry, J., Buie, M., Olkin, C., Young, E., 2010. Near-infrared spectral monitoring of Triton with IRTF/SpeX II: Spatial distribution and evolution of ices. Icarus 205, 594–604.

Hansen, C.J., Paige, D.A., 1996. Seasonal nitrogen cycles on Pluto. Icarus 120, 247–265.

Hillier, J., Helfenstein, P., Verbiscer, A., Veverka, J., Brown, R., Goguen, J., Johnson, T., 1990. Voyager disk-integrated photometry of Triton. Science 250, 419–421.

Hillier, J., Veverka, J., Helfenstein, P., 1994. Photometric diversity of terrains on Triton. Icarus 109, 296–312.

Hinson, D.P., Linscott, I.R., Young, L.A., Tyler, G.L., Stern, S.A., Beyer, R.A., Bird, M.K., Ennico, K., Gladstone, G.R., Olkin, C.B., Pätzold, M., Schenk, P.M., Strobel, D.F., Summers, M.E., Weaver, H.A., Woods, W.W., 2017. Radio occultation measurements of Pluto's neutral atmosphere with New Horizons. Icarus 290, 96–111.

Hubbard, W.B., Hunten, D., Dieters, S., Hill, K., Watson, R., 1988. Occultation evidence for an atmosphere on Pluto. Nature 336, 452.

Lisse, C., Young, L., Cruikshank, D., et al., 2019. On the stability of kbo 2014 mu69s ices. Icarus .

McKinnon, W.B., Stern, S., Weaver, H., Nimmo, F., Bierson, C., Grundy, W., Cook, J., Cruikshank, D., Parker, A., Moore, J., et al., 2017. Origin of the Pluto–Charon system: Constraints from the New Horizons flyby. Icarus 287, 2–11.

Nimmo, F., Umurhan, O., Lisse, C.M., Bierson, C.J., Lauer, T.R., Buie, M.W., Throop, H.B., Kammer, J.A., Roberts, J.H., McKinnon, W.B., Zangari, A.M., Moore, J.M., Stern, S.A., Young, L.A., Weaver, H.A., Olkin, C.B., Ennico, K., 2017. Mean radius and shape of Pluto and Charon from New Horizons images. Icarus 287, 12–29. arXiv:1603.00821.

Owen, T.C., Roush, T.L., Cruikshank, D.P., Elliot, J.L., Young, L.A., de Bergh, C., Schmitt, B., Geballe, T.R., Brown, R.H., Bartholomew, M.J., 1993. Surface ices and the atmospheric composition of Pluto. Science 261, 745–748.

Protopapa, S., Grundy, W., Reuter, D., Hamilton, D., Dalle Ore, C., Cook, J., Cruikshank, D., Schmitt, B., Philippe, S., Quirico, E., et al., 2017. Plutos global surface composition through pixel-by-pixel Hapke modeling of New Horizons Ralph/LEISA data. Icarus 287, 218–228.

Reuter, D.C., Stern, S.A., Scherrer, J., Jennings, D.E., Baer, J.W., Hanley, J., Hardaway, L., Lunsford, A., McMuldroch, S., Moore, J., et al., 2008. Ralph: A visible/infrared imager for the New Horizons Pluto/Kuiper Belt mission. Space Science Reviews 140, 129–154.

Schenk, P.M., Beyer, R.A., McKinnon, W.B., Moore, J.M., Spencer, J.R., White, O.L., Singer, K., Nimmo, F., Thomason, C., Lauer, T.R., Robbins, S., Umurhan, O.M., Grundy, W.M., Stern, S.A., Weaver, H.A., Young, L.A., Smith, K.E., Olkin, C., New Horizons Geology, Geophysics Investigation Team, 2018. Basins, fractures and volcanoes: Global cartography and topography of Pluto from New Horizons. Icarus 314, 400–433.

Schmitt, B., Philippe, S., Grundy, W., Reuter, D., Côte, R., Quirico, E., Protopapa, S., Young, L., Binzel, R., Cook, J., et al., 2017. Physical state and distribution of materials at the surface of Pluto from New Horizons LEISA imaging spectrometer. Icarus 287, 229–260.

Scott, T.A., 1976. Solid and liquid nitrogen. Physics Reports 27, 89–157. doi:10.1016/0370-1573(76)90032-6.

Spencer, J.R., Stansberry, J.A., Trafton, L.M., Young, E.F., Binzel, R.P., Croft, S.K., 1997. Volatile transport, seasonal cycles, and atmospheric dynamics on Pluto. Pluto and Charon , 435–473.

Stansberry, J., Pisano, D., Yelle, R., 1996a. The emissivity of volatile ices on Triton and Pluto. Planetary and Space Sci. 44, 945–955.

Stansberry, J., Spencer, J., Schmitt, B., Benchkoura, A., Yelle, R., Lunine, J., 1996b. A model for the overabundance of methane in the atmospheres of Pluto and Triton. Planetary and Space Sci. 44,

1051–1063.
Stansberry, J., Yelle, R., 1999. Emissivity and the Fate of Pluto's Atmosphere. Icarus 141, 299–306.
Stansberry, J.A., Grundy, W., Young, L., 2014. The Influence of Topography on Volatile Transport, in: AAS/Division for Planetary Sciences Meeting Abstracts #46, p. 401.08.
Stansberry, J.A., Yelle, R.V., Lunine, J.I., McEwen, A.S., 1992. Triton's surface-atmosphere energy balance. Icarus 99, 242–260.
Stern, S., Trafton, L., Gladstone, G., 1988. Why is Pluto bright? Implications of the albedo and lightcurve behavior of Pluto. Icarus 75, 485–498.
Stern, S.A., 2010. Solar system: Pluto is again a harbinger. Nature 468, 775–776. doi:10.1038/468775a.
Stern, S.A., Weaver, H. A., J., Young, L.A., Olkin, C., Ennico Smith, K., Moore, J.M., Spencer, J.R., McKinnon, W.B., Grundy, W.M., Cruikshank, D.P., Bagenal, F., Gladstone, R., Summers, M.E., 2015. Overview of Key Results from the Exploration of the Pluto System by New Horizons, in: AGU Fall Meeting Abstracts, pp. U53A–01.
Trafton, L., 1984. Large seasonal variations in triton's atmosphere. Icarus 58, 312–324.
Trafton, L., Stern, S., 1983. On the global distribution of Pluto's atmosphere. The Astrophysical Journal 267, 872–881.
Trafton, L.M., 2015. On the state of methane and nitrogen ice on Pluto and Triton: Implications of the binary phase diagram. Icarus 246, 197–205. doi:10.1016/j.icarus.2014.05.022.
Trafton, L.M., Stansberry, J.A., 2015. On the Departure from Isothermality of Pluto's Volatile Ice due to Local Insolation and Topography, in: AAS/Division for Planetary Sciences Meeting Abstracts.
Yelle, R.V., Lunine, J.I., Pollack, J.B., Brown, R.H., 1995. Lower atmospheric structure and surface-atmosphere interactions on Triton., in: Cruikshank, D.P., Matthews, M.S., Schumann, A.M. (Eds.), Neptune and Triton, pp. 1031–1105.
Young, L., Stansberry, J., Protopapa, S., Schmitt, B., Earle, A., Schenk, P., Howard, A., 2017. N2 in Plutos Northern Lowlands, in: European Planetary Science Congress.
Young, L.A., 2013. Pluto's seasons: New predictions for New Horizons. The Astrophysical Journal Letters 766, L22.